



# High reversible sodium insertion into iron substituted $\text{Na}_{1+x}\text{Ti}_{2-x}\text{Fe}_x(\text{PO}_4)_3$

M.J. Aragón, C. Vidal-Abarca, P. Lavela\*, J.L. Tirado

Laboratorio de Química Inorgánica, Universidad de Córdoba, Edificio Marie Curie, Campus de Rabanales, 14071 Córdoba, Spain

## HIGHLIGHTS

- $\text{Na}_{1+x}\text{Ti}_{2-x}\text{Fe}_x(\text{PO}_4)_3$  is proposed as potential electrodes for sodium batteries.
- Iron substitution revealed an anisotropic change of the cell parameters.
- Low contents of iron involved high capacity values and good capacity retention.
- Lower resistance for charge transfer and phase transition at the interphase.

## ARTICLE INFO

### Article history:

Received 24 September 2013

Received in revised form

28 November 2013

Accepted 2 December 2013

Available online 11 December 2013

### Keywords:

Sodium batteries

Intercalation reactions

Energy storage

Phosphate

NASICON

## ABSTRACT

Current research trends on energy storage have given new impetus to the development of sodium-ion batteries. In this context, titanium phosphates with a NASICON-related structure are known to provide a stable crystal structure for sodium mobility. With adequate redox centers, these materials are studied here as attractive cathodes vs. sodium. Powdered solids of general stoichiometry  $\text{Na}_{1+x}\text{Ti}_{2-x}\text{Fe}_x(\text{PO}_4)_3$  ( $0 \leq x \leq 0.8$ ) were obtained and electrochemically tested. The structural modifications induced by the substitution of  $\text{Ti}^{4+}$  by  $\text{Fe}^{3+}$  were analyzed by X-ray diffraction revealing an anisotropic change of the unit cell parameters. A continuous voltage decrease is observed between 2.6 and 2.0 V in the iron containing samples, which was ascribed to the contribution of the  $\text{Fe}^{3+}/\text{Fe}^{2+}$  redox couple, as determined by  $^{57}\text{Fe}$  Mössbauer spectroscopy. A detailed analysis of this region revealed the occurrence of local orderings of inserted sodium ions. The introduction of low contents of iron ( $x = 0.2$ ) involved a capacity value of  $130.2 \text{ mA h g}^{-1}$  after the first discharge and a good capacity retention after an extended cycling. It was correlated to the low internal resistance values for this composition.

© 2013 Elsevier B.V. All rights reserved.

## 1. Introduction

According to excellent reviews recently published, Na-ion batteries are now emerging as a serious competitor of Li-ion batteries for particular applications [1,2]. A number of reports demonstrated the reliability of sodium batteries to provide reversible energy storage devices [3–5]. Otherwise, the increasing demand of this element needed for the transportation market have pointed out the possible scarcity of lithium resources in a next future [6,7]. Sodium is an abundant and non-expensive alkali element, environmentally friendly and full recyclability. These are outstanding properties promoting the use of sodium batteries in large-scale stationary energy storage related to renewable energy and smart grids [8].

Anode materials, formerly researched for Li-ion batteries, are being revisited for their use in sodium cells. Thus, surface-modified

carbon microbeads revealed the presence of internal cavities contributing to the optimization of the electrochemical behavior [9]. These structural defects can be also induced in graphitized carbons by mechanical grinding with positive effects on the insertion of sodium [10]. Hard carbons are potential candidates, though great efforts are now being developed for diminishing the irreversibility of the first cycle. Promising results have been achieved by optimizing the electrolyte composition [11,12]. Hierarchically porous carbons [13], Carbon based hollow nanowires [14] and N-doped carbon nanosheets [15].

An increasing interest is being paid on sodium-tin alloys materials as negative electrodes [16]. Surprisingly, Wang et al. reported good cyclability of the tin based electrode which was interpreted in terms of the absence of particle cracking or fracture, despite a huge volumetric expansion of about 420% [17]. Likewise, reversible specific capacities close to the theoretical value have been achieved for micrometric Sb after a large number of cycles, outperforming the behavior of this element in lithium ion batteries

\* Corresponding author. Tel./fax: +34 957 218 637.

E-mail address: [iq1lacap@uco.es](mailto:iq1lacap@uco.es) (P. Lavela).

[18]. Also, transition metal oxides prepared as electrodeposited thin films have demonstrated a notorious improvement of the coulombic efficiency performing sodium driven conversion reactions. It was ascribed to the synergic effects of both transition metal elements along with the nano-crystalline character [19].

Layered oxides with  $\text{NaTMO}_2$  (TM: Mn, Fe, Co, Ni, etc.) stoichiometry are a large family of compounds. Their well-structured framework is more resilient to structural changes upon cycling, though are prone to absorb water molecules into the interlayer space [20–22]. The different working voltage and specific capacity associated to each transition element yields a rich electrochemistry which allows a fine tune of the energy density [23]. Recently, much effort is being put on transition metal polyanionic compounds. The strong inductive effect exerted by  $\text{PO}_4^{3-}$  polyanions with strong X–O covalence is responsible for the relatively high operating voltage [24]. Nevertheless, few examples of electrode materials others than phosphate have been reported in the literature [25]. Much effort is being put on transition metal phosphates. The large success achieved by the lithium counterpart with olivine structure has encouraged the research on  $\text{NaFePO}_4$  and related compositions [26–30]. Also, the incorporation of fluoride anions has provided promising electrode materials [31–34].

Transition metal phosphates exhibiting a NASICON-type structure are particularly interesting due to their compositional variety,  $\text{AB}_2(\text{PO}_4)_3$  (A:  $\text{Li}^+$ ,  $\text{Na}^+$ ,  $\text{Mg}^{2+}$ ,  $\text{Mn}^{2+}$ , etc; B:  $\text{Fe}^{3+}$ ,  $\text{V}^{3+}$ ,  $\text{Ti}^{4+}$ ). The framework can be described as a three-dimensional assembly of  $[\text{Ti}_2(\text{PO}_4)_3]^-$ . The structure yields octahedral  $\text{M}_1$  sites sharing faces with two adjacent  $\text{TiO}_6$  octahedra along the hexagonal *c*-axis which are fully occupied by sodium atoms in this stoichiometry. These chains are linked by  $\text{PO}_4$  tetrahedra sharing corners with  $\text{TiO}_6$  octahedra. Large octahedral  $\text{M}_2$  vacant sites are created between the  $\text{PO}_4$  tetrahedra which are interconnected to  $\text{M}_1$  sites allowing a diffusion path for the inserted alkaline ions [35,36]. Also, the rigid framework with interconnected vacant sites facilitates the insertion and fast diffusion of alkaline ions. Delmas et al. reported the reversible electrochemical sodium insertion into  $\text{NaTi}_2(\text{PO}_4)_3$  [37].

The aim of this work is the synthesis and electrochemical characterization of the  $\text{Na}_{1+x}\text{Ti}_{2-x}\text{Fe}_x(\text{PO}_4)_3$  ( $0 \leq x \leq 0.8$ ) series as potential electrode material for sodium cells. The microstructure of the pristine samples will be analyzed by X-ray diffraction and electron microscopy. The electrochemical behavior will be determined using the galvanostatic method and impedance spectroscopy.

## 2. Experimental

Samples with the nominal stoichiometry  $\text{Na}_{1+x}\text{Ti}_{2-x}\text{Fe}_x(\text{PO}_4)_3$  ( $0 \leq x \leq 0.8$ ) were synthesized by dissolving stoichiometric amounts of  $\text{NaH}_2\text{PO}_4$  (Panreac),  $\text{NH}_4\text{H}_2\text{PO}_4$  (Aldrich) and  $\text{Fe}(\text{NO}_3)_3 \cdot 9\text{H}_2\text{O}$  in deionized water. Citric acid was added in 2:1 transition metal to citrate ratio. The further thermal decomposition of this carbon source will yield a coating improving the electron conducting properties of the transition metal phosphate. An ethanol solution of titanium isopropoxide with the appropriated ratio was poured on the previous one. The hydrolysis of the Ti reagent yields a slurry which was ultrasonicated for 1 h to ensure the full mixing of the elements. The solvent was then evaporated and the solid precursor was recovered and ground. The precursor was eventually annealed in an argon atmosphere at  $750^\circ\text{C}$  for 10 h using a heating ramp of  $3^\circ\text{C min}^{-1}$ . The precise carbon content in these samples was determined by using an Elemental CHNS Eurovector EA 3000 analyser and the mass of the active material was corrected accordingly.

X-ray diffraction (XRD) patterns were scanned on a Siemens D5000 diffractometer equipped with  $\text{CuK}\alpha$  radiation and a graphite

monochromator. The samples were scanned between  $10$  and  $110^\circ$  ( $2\theta$  degrees) in a step scan mode ( $0.04^\circ$  steps/12 s). Unit cell parameters were calculated with *Fullprof* software. Scanning electron microscopy (SEM) and energy dispersive spectroscopy (EDS) analysis were carried out in a JEOL JSM63000 microscope. Transmission electron microscopy (TEM) images were recorded in a JEOL 200CX microscope.

The cycling performance of sodium cells was monitored in two-electrode Swagelok™ type cells assembled in a glove box under a controlled argon atmosphere. For this purpose, the working electrodes were prepared by mixing the active material (80%), carbon black (10%) and PVDF (10%) (polyvinylidene fluoride) in *N*-methyl-2-pyrrolidone. To ensure a proper homogenization, the slurry was vigorously stirred in an Ultraturrax disperser at 10,000 rpm. The electrode material was cast onto a 9 mm aluminum collectors and vacuum dried at  $120^\circ\text{C}$  for at least 2 h. A 9 mm sodium disk was used as a counter electrode. The electrolyte solution was 1 M  $\text{NaPF}_6$  (EC:DEC) (1%VC) soaked in glass fiber separators (GF/A-Whatman). The test cells were galvanostatically cycled between 1.7 and 3.6 V. The charge and discharge rates will be expressed as  $C/n$ , being *n* the number of hours needed for the insertion of one sodium per formula unit at the applied current intensity. Potentiostatic Intermittent Titration Technique (PITT) was performed in a VMP system applying 1.5 mV potential steps. The relaxation current was limited to  $0.6 \mu\text{A}$ . Electrochemical Impedance Spectra (EIS) were recorded on an Autolab PGSTAT12. Three-electrode Swagelok™ type cells were cycled up to the end of the *n*<sup>th</sup> discharge and let to relax at open circuit voltage for at least 12 h to achieve a quasi-equilibrium state. A sodium disk was used as a reference electrode. The impedance spectra were recorded on by perturbing the equilibrium potential with an AC voltage signal of 5 mV from 100 kHz to 2 mHz.

## 3. Results and discussions

XRD patterns of  $\text{Na}_{1+x}\text{Ti}_{2-x}\text{Fe}_x(\text{PO}_4)_3$  ( $0 \leq x \leq 0.8$ ) series are displayed in Fig. 1. The observed reflections were indexed in the R-3c space group of the trigonal system (rhombohedral Bravais lattice) as previously reported for  $\text{NaTi}_2(\text{PO}_4)_3$  [37]. The substitution of  $\text{Ti}^{4+}$  by  $\text{Fe}^{3+}$  ions involves the incorporation of additional  $\text{Na}^+$  ions to counteract the diminution in positive charge of the transition metal. The cell parameters calculated from the indexed pattern are included in Table 1. Because of  $\text{M}_1$  sites are fully occupied, the additional sodium existing in the iron containing samples must be

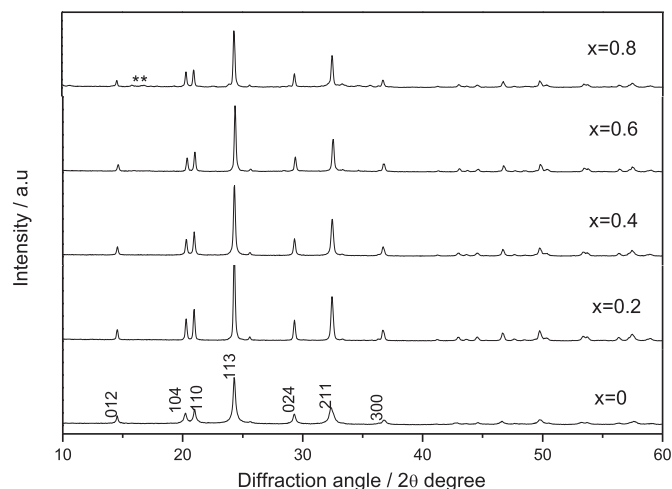


**Fig. 1.** X-ray diffraction patterns of  $\text{Na}_{1+x}\text{Ti}_{2-x}\text{Fe}_x(\text{PO}_4)_3$  for  $x = 0.0, 0.2, 0.4, 0.6$  and  $0.8$ . Miller indices have been annotated. Asterisks denote small reflections belonging to impurities.

**Table 1**

Cell parameters in the R-3c space group for the  $\text{Na}_{1+x}\text{Ti}_{2-x}\text{Fe}_x(\text{PO}_4)_3$  ( $0.0 \leq x \leq 0.6$ ) samples and P/Fe and Ti/Fe atomic ratio measured by EDS.

$x$	$a/\text{\AA}$	$c/\text{\AA}$	$c/a$	P/Fe	Ti/Fe
0.0	8.4587(6)	21.954(2)	2.5954	–	–
0.2	8.4837(2)	21.832(1)	2.5734	15.19	8.85
0.4	8.4838(3)	21.825(1)	2.5725	7.69	3.94
0.6	8.4874(2)	21.809(1)	2.5695	4.67	2.34

allocated in the  $\text{M}_2$  sites. It is reflected by a slight increase of  $a$ , while  $c$  decreases, hence decreasing the  $c/a$  ratio. This result matches well with the tendency reported elsewhere [38]. Attempts of increasing the iron content over  $x = 0.6$  led to a non-negligible contribution of impurities as  $\text{NaFeP}_2\text{O}_7$  (JCPDS 23-0681) and  $\text{Fe}_4(\text{P}_2\text{O}_7)_3$  (JCPDS 36-0318), marked with an asterisk in Fig. 1. Even if the  $\text{Na}_2\text{TiFe}(\text{PO}_4)_3$  has been reported [38], the lower temperature of annealing employed in this work to ensure the proper formation of the conductive carbon phase may limit the incorporation of iron over  $x = 0.6$ . For this reason, samples with  $x > 0.6$  were discarded in this study.

The analysis of the SEM micrographs of these samples (Fig. 2a) shows large aggregates of primary particles mutually interconnected as a common feature for all compositions. These assemblies generate a macroporous system which undoubtedly favors the impregnation with the electrolyte. TEM images offer a close inspection of the microstructural properties of these samples.

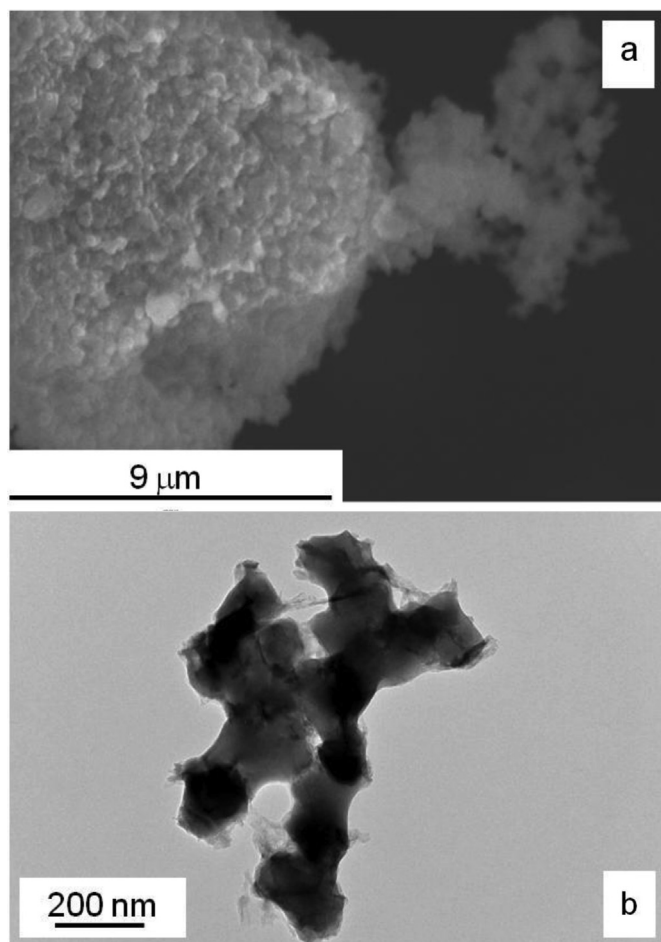


**Fig. 2.** a) Scanning electron micrograph of  $\text{Na}_{1.2}\text{Ti}_{1.8}\text{Fe}_{0.2}(\text{PO}_4)_3$  and b) Transmission electron micrograph of  $\text{Na}_{1.6}\text{Ti}_{1.4}\text{Fe}_{0.6}(\text{PO}_4)_3$ .

As an example, Fig. 2b shows an isolated small aggregate of  $\text{Na}_{1.6}\text{Ti}_{1.4}\text{Fe}_{0.6}(\text{PO}_4)_3$  in which nanometric particles with irregular shape and size are merged. Lamellar carbon particles appear attached to the surface to provide a good electrical contact among the grains of the electro-active material. The preparation procedure involves the complete evaporation of the solvent and the full recovery of the solid precursor prior to annealing. Thus, the composition of the final product is expected to be coincident with that of the precursor. Table 1 includes EDS results evidencing that the experimental P/Fe and Ti/Fe atomic ratios agree well with the theoretical stoichiometries.

The first report on the sodium insertion in  $\text{Na}_{2+x}\text{TiFe}(\text{PO}_4)_3$  obtained by solid state reaction describes a two-phase region between  $0 \leq x \leq 0.5$  [39]. It was interpreted as a local ordering induced by the ion–ion interactions that distribute the cations to minimize the coulombic potential energy. For  $x > 1$ , a rapid decrease of potential was observed due to the high electrostatic repulsions between intercalated cations [39]. A more recent study on this composition, similarly prepared by the solid state reaction route, revealed a quite different profile. The charge and discharge curve was ascribed to a single-phase reaction all along the insertion domain. It was demonstrated by the current decay in PITT mode and the continuous shift of the diffraction peaks of the *in situ* XRD patterns [39]. These different interpretations reveal the complexity of the sodium insertion mechanism in this system. Most likely, it is affected by other factors than composition as for instance crystallinity and particle size among others.

Voltage versus composition plots for the first cycle are displayed in Fig. 3. The reference  $\text{NaTi}_2(\text{PO}_4)_3$  sample shows an extended plateau at 2 V which has been attributed to a two phase mechanism in which both  $\text{NaTi}_2(\text{PO}_4)_3$  and  $\text{Na}_3\text{Ti}_2(\text{PO}_4)_3$  are involved [37]. On increasing the iron content, a new region progressively appears between 2.0 and 3.6 V when the cell is discharged at C/10. This electrochemical feature is characterized by a continuous voltage decrease until the flat plateau is reached at 2 V. This curve shape could be correlated to a solid solution mechanism. A PITT experiment was carried out on the  $\text{Na}_{1.6}\text{Ti}_{1.4}\text{Fe}_{0.6}(\text{PO}_4)_3$  sample (Fig. 4). A close inspection of the quasi-equilibrium curve recorded on the first discharge in the range  $0 < y < 0.6$  reveals that the mechanism cannot be exclusively attributed to a solid solution. The presence of successive small plateaus located at  $y = 0.02, 0.09, 0.27, 0.35, 0.52$  and  $0.43$ , appearing as bell-shaped current relaxation curves, are characteristic of local orderings when sodium is inserted at those compositions (Fig. 4). Therefore, the insertion of sodium ions in the studied samples involves ionic interactions among the alkali ions inserted at the  $\text{M}_2$  sites. These local orderings are limited to very short composition ranges. The coulombic efficiency was calculated from the discharge and charge capacities recorded during the first ten cycles at C/10 and the results are included in Fig. 5. A low value of only 84% was determined for the iron free sample after the first cycle, though an increase was observed for further cycles. Otherwise, samples containing iron revealed efficiency values higher than 94% since the first cycles. These high values were kept at least for the first ten cycles. Efficiency results for a larger number of cycles will be commented below at the light of Fig. 7.

$^{57}\text{Fe}$  Mössbauer spectra of partially discharged and subsequently charged  $\text{Na}_{1.4}\text{Ti}_{1.6}\text{Fe}_{0.4}(\text{PO}_4)_3$  electrodes were recorded at room temperature to monitor the role of the  $\text{Fe}^{3+}/\text{Fe}^{2+}$  redox couple during the electrochemical insertion/extraction of sodium (Fig. 6). The pristine material shows a split signal located at ca.  $0.39 \text{ mm s}^{-1}$  and a quadrupole splitting value of  $0.77 \text{ mm s}^{-1}$ , which are clearly attributed to the presence of  $\text{Fe}^{3+}$  (Table 2). This quadrupole splitting value is slightly lower than that recently reported for a closely related lithium containing phosphate [40]. It is indicative of a more isotropic local environment surrounding the iron probe

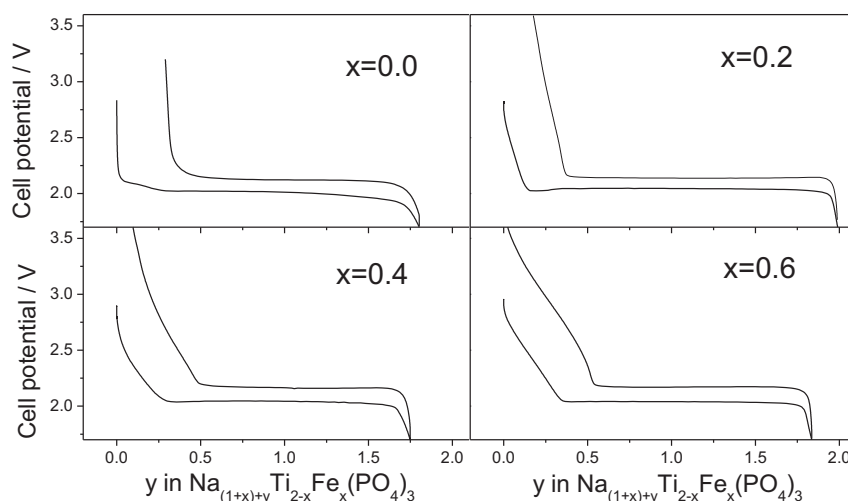


Fig. 3. Voltage versus capacity curves recorded after the first cycles for the studied samples. Sodium cells were subjected to a C/10 rate.

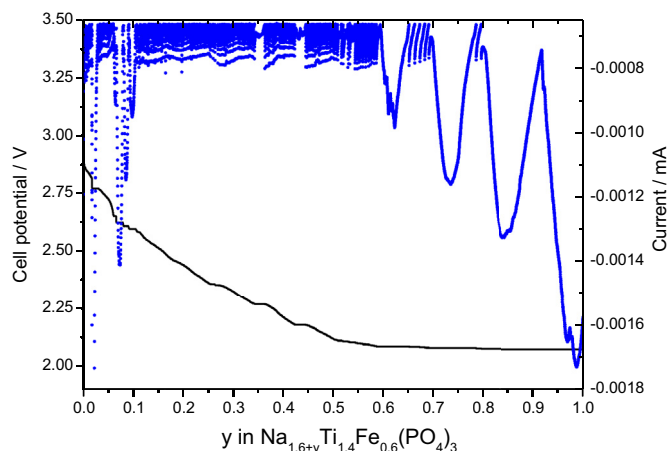


Fig. 4. Step potential curve for  $\text{Na}_{1.6+y}\text{Ti}_{1.4}\text{Fe}_{0.6}(\text{PO}_4)_3$  in the range between  $0 \leq y \leq 1$ .

atoms in the sodium compound. In order to determine the region at which trivalent iron is reduced, an electrode was partially discharged at  $x = 1$ . The spectra profile can be interpreted in terms of two different doublets signals ascribable to  $\text{Fe}^{3+}$  and  $\text{Fe}^{2+}$ . The

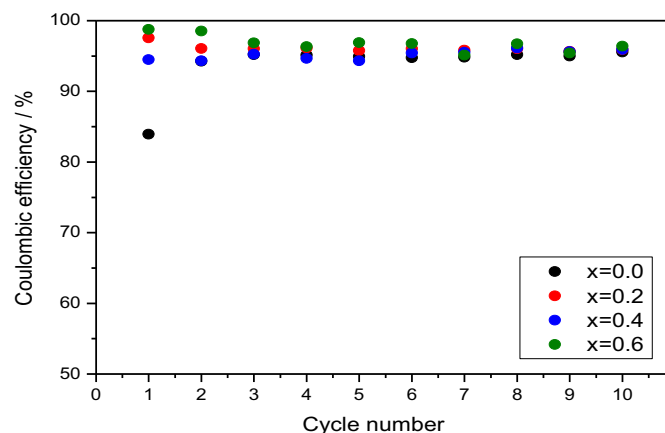


Fig. 5. Plot of the coulombic efficiencies recorded for cells assembled with  $\text{Na}_{1+x}\text{Ti}_{2-x}\text{Fe}_x(\text{PO}_4)_3$  ( $x = 0.0, 0.2, 0.4, 0.6$ ) and cycled at C/10.

latter signal is characterized by an isomer shift of  $1.13 \text{ mm s}^{-1}$  and a quadrupole splitting of  $2.26 \text{ mm s}^{-1}$  (Table 2). The contribution of this doublet accounted for 79% of the overall spectrum, evidencing that iron reduction predominantly undergoes in this first voltage region. Minor contributions of  $\text{Fe}^{3+}$  to this spectrum can be associated to kinetic restriction during the cell discharge at C/10 which prevents the full reduction of the ferric cations. After the full discharge at 1.7 V, only the highly split doublet ascribed to  $\text{Fe}^{2+}$  could be observed, evidencing the efficient contribution of the  $\text{Fe}^{3+}/\text{Fe}^{2+}$  redox couple to the electrochemical insertion of sodium. On cell charging, a spectrum was recorded on an electrode partially charged at  $x = 1$ . The occurrence of a unique highly split signal

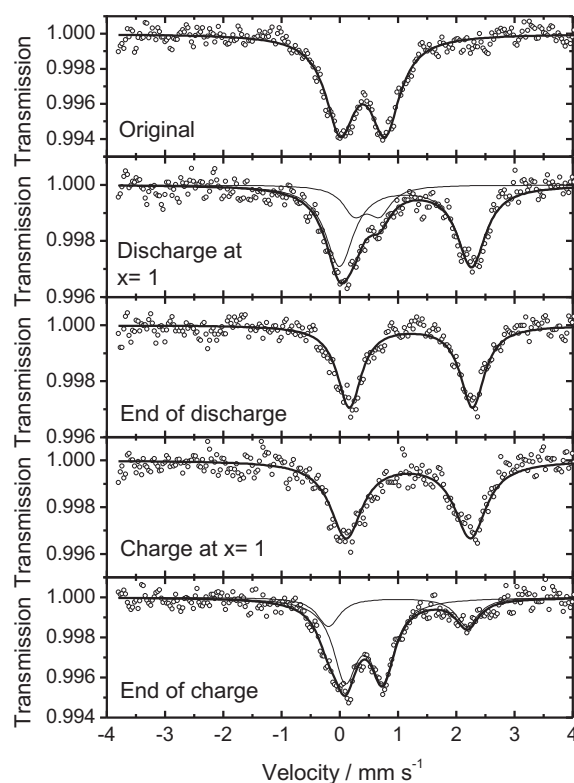
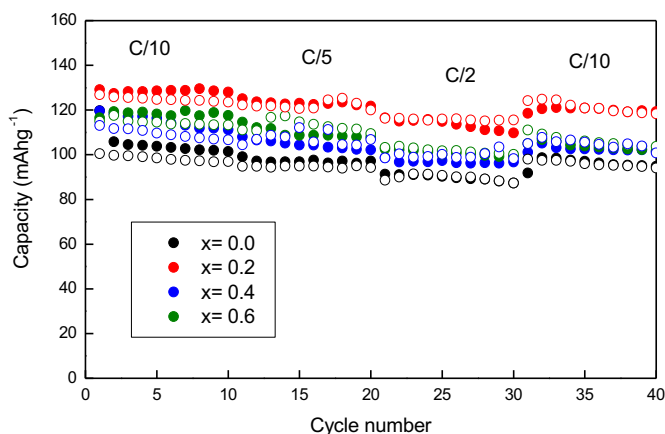


Fig. 6. Ex-situ  $^{57}\text{Fe}$  Mössbauer spectra of pristine  $\text{Na}_{1.4}\text{Ti}_{1.6}\text{Fe}_{0.4}(\text{PO}_4)_3$  sample and partially discharged and subsequent charged electrodes during the first cycle. The cells were discharged at C/20.





**Fig. 7.** Capacity versus the number of cycles of sodium cells assembled with  $\text{Na}_{1+x}\text{Ti}_{2-x}\text{Fe}_x(\text{PO}_4)_3$  ( $0.0 \leq x \leq 0.6$ ). Discharge and charge capacity values are respectively depicted by closed and open symbols.

clearly ascribable to  $\text{Fe}^{2+}$  evidences the preferential electrochemical activity of the iron redox couple at high voltages, while titanium reacts along the extended plateau at ca. 2 V. Finally, a Mössbauer spectrum was recorded on a fully charged electrode. A low split signal of  $\text{Fe}^{3+}$  appears at  $0.416 \text{ mm s}^{-1}$  with a contribution of 74%, while a small signal of  $\text{Fe}^{2+}$  at  $0.996 \text{ mm s}^{-1}$  remain visible, probably due to kinetic restrictions in this high voltage region.

The cycling behavior of the electrodes was evaluated at increasing rates of C/10, C/5 and C/2, and eventually decreasing to C/10 for the last cycles. Fig. 7 shows the discharge (closed symbols) and charge (open symbols) capacity values. An enhanced irreversibility is observed after the first cycle in  $\text{NaTi}_2(\text{PO}_4)_3$ . The initial discharge capacity value of  $120 \text{ mA h g}^{-1}$  was diminished to  $106 \text{ mA h g}^{-1}$  for the second cycle. The latter value is close to that reported for a related  $\text{Na}_3\text{Ti}_2(\text{PO}_4)_3$  phase [41]. Coulombic efficiency can be calculated from charge and discharge capacity values for each cycle. Thus, the initial irreversibility clearly affect to this value which is diminished to 79% after 40 cycles at different rates. On substituting Ti by Fe, we observe an improvement of the reversibility after the first cycle. Thus, the coulombic efficiency after 40 cycles was as high as 91, 87 and 85% for samples with  $x = 0.2, 0.4$  and  $0.6$ , respectively. The highest discharge capacity values were recorded for the sample with  $x = 0.2$ . In this case, a capacity value of  $130.2 \text{ mA h g}^{-1}$  was determined after the first discharge, which is very close to the maximum theoretical value expected for this stoichiometry ( $130.8 \text{ mA h g}^{-1}$ ). Nevertheless, further substitution of Ti by Fe, with the consequent introduction of additional sodium to counterbalance the positive charge, led to a decrease of capacity. Thus, discharge capacity values of  $119.4$  and  $116.6 \text{ mA h g}^{-1}$  were respectively recorded after the first discharge for samples with  $x = 0.4$  and  $0.6$ .

**Table 2**

Hyperfine parameters of the deconvoluted  $^{57}\text{Fe}$  Mössbauer spectra of the  $\text{Na}_{1.4}\text{Ti}_{1.6}\text{Fe}_{0.4}(\text{PO}_4)_3$  sample and partially discharged and charged electrodes.

Sample	$\delta$ ( $\text{mm s}^{-1}$ )	$\Delta$ ( $\text{mm s}^{-1}$ )	$\Gamma$ ( $\text{mm s}^{-1}$ )	C (%)	$\chi^2$
Original	0.39(1)	0.77(1)	0.61(2)	100	0.693
Discharge at $x = 1$	0.46(4)	0.43(4)	0.47(9)	21	0.469
	1.13(1)	2.26(2)	0.59(3)	79	
End of discharge	1.22(1)	2.12(2)	0.50(2)	100	0.601
Charge at $x = 1$	1.18(1)	2.13(2)	0.66(3)	100	0.578
End of charge	0.42(1)	0.64(1)	0.50(2)	74	0.568
	1.00(2)	2.38(4)	0.47(6)	26	

$\delta$ : isomer shift;  $\Delta$ : quadrupolar splitting;  $\Gamma$ : line-width at half maximum; C: contribution/concentration;  $\chi^2$ : goodness of the fitting.

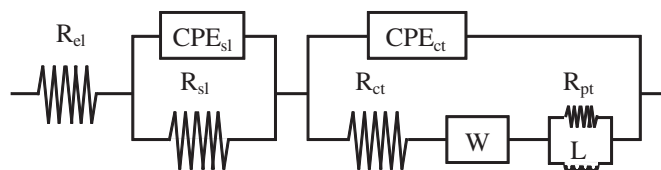


**Fig. 8.** Equivalent circuit employed to the fitting of the impedance spectra.

Impedance spectroscopy allows determining the internal cell resistances responsible for the kinetic response of the working electrodes under operation. This parameter may clarify the electrode performance observed when the electrode materials are cycled for a number of cycles at progressively high C rates, as shown in Fig. 7. Nyquist plots recorded for selected samples ( $x = 0.0, 0.2$  and  $0.6$ ) are characterized by two depressed overlapped semicircles at high and medium frequencies. These features are commonly attributed to the ion migration through the surface layer (sl) and the charge transfer process (ct) when are transferred from the electrolyte towards the bulk of the particle. Additionally, an inductive loop appears at low frequencies (Supplementary data). This feature has been interpreted as a result of the diffusion of the alkali ions in a two phase system, existing in a core-shell particle. This phenomenon will be affected by both the relaxation occurring at the shell phase and the phase transformation relaxation process from core phase. The inductive loop is a consequence of the coupling of both relaxations in the high frequency region of diffusion impedance according to the theoretical calculation [42,43]. The fitting of the spectra was carried out using the model proposed in Fig. 8. The resistance  $R_{el}$  refers to the ionic resistance of the electrolyte.  $R_{sl}$  simulates the resistance at the surface layer on the electrode.  $R_{ct}$  is set for the impedance of charge-transfer reaction. The CPE elements describe the capacitive behavior at the interphases. Because of electrode roughness and inhomogeneous reactions, the semicircles are depressed. In this case, capacitors are substituted by these elements allowing a better fitting of the spectra.  $W$  represents diffusion impedance. Eventually, a resistance ( $R_{pt}$ ) paralleled to an inductance  $L$  allows to describe the phase transformation [43]. The resistance values for selected samples have been written in Table 3. The analysis of these values allow us to infer a close relationship between the highest coulombic efficiency of sample with  $x = 0.2$  (88%) after the cycling at a C/2 rate and the lowest internal impedance recorded for this sample. After a number of cycles, we observe a notorious increase of the electrode impedance for samples with  $x = 0$  and  $0.6$ . This variation is more abrupt for  $\text{Na}_{1.6}\text{Ti}_{1.4}\text{Fe}_{0.6}(\text{PO}_4)_3$ , while a progressive of the resistance is detected for  $\text{NaTi}_2(\text{PO}_4)_3$ . In contrast, a moderate increase of the electrode impedance was measured for the sample with  $x = 0.2$ .

**Table 3**

Resistance values calculated from the impedance spectra of  $\text{Na}_{1+x}\text{Ti}_{2-x}\text{Fe}_x(\text{PO}_4)_3$  electrodes after the first, fifth, tenth and fiftieth discharges.

$x$ in $\text{Na}_{1+x}\text{Ti}_{2-x}\text{Fe}_x(\text{PO}_4)_3$	$n^{\text{th}}$ discharge	$R_{el}$	$R_{sl}$	$R_{ct}$	$R_{pt}$
$x = 0$	1 <sup>st</sup>	0.004	0.113	0.200	0.067
	5 <sup>th</sup>	0.004	0.321	0.124	0.055
	10 <sup>th</sup>	0.004	0.214	0.355	0.084
	50 <sup>th</sup>	0.006	0.514	0.162	—
$x = 0.2$	1 <sup>st</sup>	0.003	0.142	0.053	0.031
	5 <sup>th</sup>	0.004	0.127	0.077	0.033
	10 <sup>th</sup>	0.004	0.166	0.111	—
	50 <sup>th</sup>	0.007	0.106	0.285	0.051
$x = 0.6$	1 <sup>st</sup>	0.005	0.074	0.290	0.044
	5 <sup>th</sup>	0.005	0.029	0.411	0.040
	10 <sup>th</sup>	0.004	0.634	0.072	0.038
	50 <sup>th</sup>	0.012	0.521	0.140	—

after 50 cycles. The main contribution to the cell impedance on the former samples after a large number of cycles arise from the surface layer, while this value remained low for  $\text{Na}_{1.2}\text{Ti}_{1.8}\text{Fe}_{0.2}(\text{PO}_4)_3$ . Thus, the moderate changes of the surface layer resistance at the core–shell interphase were essential for preserving a stable cyclability over a large number of cycles.

#### 4. Conclusions

Titanium phosphates with a NASICON-related structure are known to provide a stable crystal structure for sodium diffusion. By adept addition of redox centers to their composition, these environmentally benign materials are studied here as potential cathodes in sodium ion batteries. Powdered solids of general stoichiometry  $\text{Na}_{1+x}\text{Ti}_{2-x}\text{Fe}_x(\text{PO}_4)_3$  ( $0 \leq x \leq 0.8$ ) were obtained by a sol–gel route including citric acid as a reagent to promote the homogeneous dispersion of metal elements and as carbon source in the final product. The substitution of  $\text{Ti}^{4+}$  by  $\text{Fe}^{3+}$  ions and the incorporation of additional  $\text{Na}^+$  ions involves a slight increase of  $a$ , while  $c$  decreases. Larger contents of iron could not be achieved because of the appearance of a non-negligible contribution of impurities in the conditions of the synthesis. The electron micrographs evidenced the benefits of the preparation route for obtaining interconnected nanometric particles of the active material properly coated with lamellar carbon particles.

Two voltage regions are discerned from the discharge curves. A continuous voltage decrease is observed between 2.6 and 2.0 V, which extent is directly related to the iron content. It was evidenced by the analysis of the iron oxidation state in partially discharged and subsequently charged electrodes by using  $^{57}\text{Fe}$  Mössbauer spectroscopy. A close inspection of the quasi-equilibrium experiments at this voltage region revealed the presence of a number of successive small plateaus which points out to the occurrence of local orderings limited to short composition ranges. Eventually, an extended flat plateau at 2.0 V was ascribed to  $\text{Ti}^{4+}$  reduction through a two phase mechanism.

The analysis of the electrochemical performance of the studied samples revealed that the introduction of low content of iron ( $x = 0.2$ ) is beneficial for achieving unexpectedly high capacity values and good capacity retention under different kinetic regimes. Thus, a capacity value of  $130.2 \text{ mA h g}^{-1}$  was recorded after the first discharge of the latter sample with a good capacity retention even at C/2 rate. The EIS results between reveal particularly low resistance values for this composition.

#### Acknowledgments

The authors are grateful to Junta de Andalucía for financial support (Contract FQM-6017) and MICINN (MAT2011-22753). We thank SCAI (UCO Central Service for Research Support) and MCYT.

#### Appendix A. Supplementary data

Supplementary data related to this article can be found at <http://dx.doi.org/10.1016/j.jpowsour.2013.12.006>.

#### References

- [1] V. Palomares, M. Casas-Cabanas, E. Castillo-Marínez, M.H. Hanb, T. Rojo, *Energy Environ. Sci.* 6 (2013) 2312–2337.
- [2] V. Palomares, P. Serras, I. Villaluenga, K.B. Hueso, J. Carretero-González, T. Rojo, *Energy Environ. Sci.* 5 (2012) 5884–5901.
- [3] M.M. Doeff, Y. Ma, S.J. Visco, L.C. De Jonghe, *J. Electrochem. Soc.* 140 (1993) L169–L170.
- [4] M.E. Spahr, P. Novak, O. Haas, R. Nesper, *J. Power Sources* 54 (1995) 346–351.
- [5] S. Bach, M. Millet, J.P. Pereira-Ramos, L. Sanchez, P. Lavela, J.L. Tirado, *Electrochem. Solid-State Lett.* 2 (1999) 545–546.
- [6] J.M. Tarascon, *Nat. Chem.* 2 (2010) 510.
- [7] C. Wadia, P. Albertus, V. Srinivasan, *J. Power Sources* 196 (2011) 1593–1598.
- [8] Brian L. Ellis, Linda F. Nazar, *Curr. Opin. Solid State Mater. Sci.* 16 (2012) 168–177.
- [9] R. Alcántara, G.F. Ortiz, P. Lavela, J.L. Tirado, *Chem. Mater.* 18 (2006) 2293–2301.
- [10] R. Alcántara, P. Lavela, G.F. Ortiz, J.L. Tirado, R. Menéndez, R. Santamaría, J.M. Jiménez-Mateos, *Carbon* 41 (2003) 3003–3013.
- [11] A. Ponrouch, R. Dedryvère, D. Monti, A.E. Demet, J.M. Ateba Mba, L. Croguennec, C. Masquelier, P. Johansson, M. Rosa Palacín, *Energy Environ. Sci.* 6 (2013) 2361–2369.
- [12] S. Komaba, W. Murata, T. Ishikawa, N. Yabuuchi, T. Ozeki, T. Nakayama, A. Ogata, K. Gotoh, K. Fujiwara, *Adv. Funct. Mater.* 21 (2011) 3859–3867.
- [13] S. Wenzel, T. Hara, J. Janek, P. Adelhelm, *Energy Environ. Sci.* 4 (2011) 3342–3345.
- [14] Y. Cao, L. Xiao, M.L. Sushko, W. Wang, B. Schwenzer, J. Xiao, Z. Nie, L.V. Saraf, Z. Yang, J. Liu, *Nano Lett.* 12 (2012) 3783–3787.
- [15] H. Wang, Z. Wu, F. Meng, D. Ma, X. Huang, L. Wang, X. Zhang, *ChemSusChem* 6 (2013) 56–60.
- [16] V.L. Chevrier, G. Ceder, *J. Electrochem. Soc.* 158 (2011) A1011–A1014.
- [17] J.W. Wang, X.H. Liu, S.X. Mao, J.Y. Huang, *Nano Lett.* 12 (2012) 5897–5902.
- [18] A. Darwiche, C. Marino, M.T. Sougrati, B. Fraisse, L. Stievano, L. Monconduit, *J. Am. Chem. Soc.* 134 (2012) 20805–20811.
- [19] M.C. López, P. Lavela, G.F. Ortiz, J.L. Tirado, *Electrochem. Commun.* 27 (2013) 152–155.
- [20] M. D'Arienzo, R. Ruffo, R. Scotti, F. Morazzoni, C.M. Mari, S. Polizzi, *Phys. Chem. Chem. Phys.* 14 (2012) 5945–5952.
- [21] S. Komaba, N. Yabuuchi, T. Nakayama, A. Ogata, T. Ishikawa, I. Nakai, *Inorg. Chem.* 51 (2012) 6211–6220.
- [22] D. Kim, E. Lee, M. Slater, W. Lu, S. Rood, C.S. Johnson, *Electrochem. Commun.* 18 (2012) 66–69.
- [23] N. Yabuuchi, M. Kajiyama, J. Iwatate, H. Nishikawa, S. Hitomi, R. Okuyama, R. Usui, Y. Yamada, S. Komaba, *Nat. Mater.* 11 (2012) 512–517.
- [24] A. Yamada, S.C. Chung, K. Hinokuma, *J. Electrochem. Soc.* 148 (2001) A224–A229.
- [25] P. Senguttuvan, G. Rousse, H. Vezin, J.-M. Tarascon, M.R. Palacín, *Chem. Mater.* 25 (2013) 2391–2393.
- [26] S.M. Oh, S.T. Myung, J. Hassoun, B. Scrosati, Y.K. Sun, *Electrochem. Commun.* 22 (2012) 149–152.
- [27] L.S. Plashnitsa, E. Kobayashi, Y. Noguchi, S. Okada, J.-I. Yamaki, *J. Electrochem. Soc.* 157 (2010) A536–A543.
- [28] K. Trad, D. Carlier, L. Croguennec, A. Wattiaux, M. Ben Amara, C. Delmas, *Chem. Mater.* 22 (2010) 5554–5562.
- [29] P. Moreau, D. Guyomard, J. Gaubicher, F. Boucher, *Chem. Mater.* 22 (2010) 4126–4128.
- [30] P. Barpanda, S. Nishimura, A. Yamada, *Adv. Energy Mater.* 2 (2012) 841–859.
- [31] N. Recham, J.N. Chotard, L. Dupont, K. Djellab, M. Armand, J.M. Tarascon, *J. Electrochem. Soc.* 156 (2009) A993–A999.
- [32] L. Brian, W.R. Ellis, M. Makahnouk, W.N. Rowan-Weatallukut, D.H. Ryan, L.F. Nazar, *Chem. Mater.* 22 (2010) 1059–1070.
- [33] P. Serras, V. Palomares, A. Goni, I. Gil de Muro, P. Kubiak, L. Lezama, T. Rojo, *J. Mater. Chem.* 22 (2012) 22301–22308.
- [34] C. Vidal-Abarca, P. Lavela, J.L. Tirado, A.V. Chadwick, M. Alfredsson, E. Kelder, *J. Power Sources* 197 (2012) 314–318.
- [35] D. Tran Qui, S. Hamdoune, J.L. Soubeyroux, E. Prince, *J. Solid State Chem.* 72 (1988) 309–315.
- [36] J.B. Goodenough, H.Y.P. Hong, J.A. Kafalas, *Mater. Res. Bull.* 11 (1976) 203–220.
- [37] C. Delmas, F. Cherkaoui, A. Nadiri, P. Hagenmuller, *Mater. Res. Bull.* 22 (1987) 631–639.
- [38] S. Patoux, G. Rousse, J.B. Leriche, C. Masquelier, *Chem. Mater.* 15 (2003) 2084–2093.
- [39] O. Tillement, J. Angenault, J.C. Couturier, M. Quarton, *Solid State Ionics* 53–56 (1992) 391–399.
- [40] C. Vidal-Abarca, P. Lavela, M.J. Aragón, N. Pyláhan, J.L. Tirado, *J. Mater. Chem.* 22 (2012) 21602–21607.
- [41] P. Senguttuvan, G. Rousse, M.E. Arroyo y de Dompablo, H. Vezin, J.M. Tarascon, M.R. Palacín, *J. Am. Chem. Soc.* 135 (2013) 3897–3903.
- [42] J. Bisquet, H. Randriamahazaka, G. García-Belmonte, *Electrochim. Acta* 51 (2005) 627–640.
- [43] J. Hong, C. Wang, U. Kasavajjula, *J. Power Sources* 162 (2006) 1289–1296.